European Journal of Radiology 170 (2024) 111257

Contents lists available at ScienceDirect

European Journal of Radiology

journal homepage: www.elsevier.com/locate/ejrad

Identification of IDH and TERTp mutations using dynamic susceptibility contrast MRI with deep learning in 162 gliomas

Buse Buz-Yalug [a], Gulce Turhan [a], Ayse Irem Cetin [a], Sukru Samet Dindar [b], Ayca Ersen Danyeli [c,d], Cengiz Yakicier [e], M. Necmettin Pamir [d,f], Koray Özduman [d,f], Alp Dincer [d,g], Esin Ozturk-Isik [a,d,*]

[a] Institute of Biomedical Engineering, Bogazici University, Istanbul, Turkey
[b] Electrical and Electronics Engineering Department, Bogazici University, Istanbul, Turkey
[c] Department of Medical Pathology, Acibadem University, Istanbul, Turkey
[d] Center for Neuroradiological Applications and Research, Acibadem University, Istanbul, Turkey
[e] Department of Molecular Biology and Genetics, Acibadem University, Istanbul, Turkey
[f] Department of Neurosurgery, Acibadem University, Istanbul, Turkey
[g] Department of Radiology, Acıbadem University, Istanbul, Turkey

ARTICLE INFO

Keywords:
Dynamic susceptibility contrast MRI
Deep learning
Attention mechanism
Glioma
Isocitrate dehydrogenase
Telomerase reverse transcriptase promoter

ABSTRACT

Purpose: Isocitrate dehydrogenase (IDH) and telomerase reverse transcriptase gene promoter (TERTp) mutations play crucial roles in glioma biology. Such genetic information is typically obtained invasively from excised tumor tissue; however, these mutations need to be identified preoperatively for better treatment planning. The relative cerebral blood volume (rCBV) information derived from dynamic susceptibility contrast MRI (DSC-MRI) has been demonstrated to correlate with tumor vascularity, functionality, and biology, and might provide some information about the genetic alterations in gliomas before surgery. Therefore, this study aims to predict IDH and TERTp mutational subgroups in gliomas using deep learning applied to rCBV images.

Method: After the generation of rCBV images from DSC-MRI data, classical machine learning algorithms were applied to the features obtained from the segmented tumor volumes to classify IDH and TERTp mutation subgroups. Furthermore, pre-trained convolutional neural networks (CNNs) and CNNs enhanced with attention gates were trained using rCBV images or a combination of rCBV and anatomical images to classify the mutational subgroups.

Results: The best accuracies obtained with classical machine learning algorithms were 83 %, 68 %, and 76 % for the identification of IDH mutational, TERTp mutational, and TERTp-only subgroups, respectively. On the other hand, the best-performing CNN model achieved 88 % accuracy (86 % sensitivity, 91 % specificity) for the IDH-mutational subgroups, 70 % accuracy (73 % sensitivity and 67 % specificity) for the TERTp-mutational subgroups, and 84 % accuracy (86 % sensitivity, 81 % specificity) for the TERTp-only subgroup using attention gates.

Conclusions: DSC-MRI can be utilized to noninvasively classify IDH- and TERTp-based molecular subgroups of gliomas, facilitating preoperative identification of these genetic alterations.

Abbreviations: IDH, isocitrate dehydrogenase; TERTp, telomerase reverse transcriptase promoter; MRI, magnetic resonance imaging; DSC-MRI, dynamic susceptibility contrast magnetic resonance imaging; rCBV, relative cerebral blood volume; CNN, convolutional neural network; GradCAM, gradient-weighted class activation mapping; NAWM, normal appearing white matter; ROI, region of interest; WHO, World Health Organization; AI, artificial intelligence. ROC, receiver operator characteristics; AUC, area under the ROC curve.

* Corresponding author at: Boğaziçi University, Institute of Biomedical Engineering, Kandilli Campus, Kandilli Mah Rasathane Cad 34684 Cengelkoy, Istanbul, Turkey.

E-mail address: esin.ozturk@boun.edu.tr (E. Ozturk-Isik).

https://doi.org/10.1016/j.ejrad.2023.111257
Received 10 July 2023; Received in revised form 21 November 2023; Accepted 6 December 2023
Available online 13 December 2023

1. Introduction

Gliomas are the most common primary malignant tumors of the central nervous system with several tumor subgroups [1]. Recently, molecular markers, such as isocitrate dehydrogenase (IDH) and telomerase reverse transcriptase gene promoter (TERTp), have been reported as significant factors that affect the prognosis of gliomas [2,3]. IDH mutations are associated with increased production of a metabolite called 2-hydroxyglutarate (2-HG) [4]. Increased levels of 2-HG inhibit the activity of proangiogenic factors, which are responsible for promoting the growth of new blood vessels. Consequently, IDH-mutant (IDH-mut) gliomas tend to exhibit reduced angiogenesis, and they have been reported to have a better response to treatment and longer overall survival than IDH wildtype (IDH-wt) gliomas [5,6]. On the other hand, TERTp mutations result in enhanced telomerase activity and lengthened telomeres which are associated with the aggressiveness of gliomas [7]. Moreover, IDH-wt gliomas with the TERTp mutation (TERTp-only) have been reported to have the worst overall survival rates [2,8]. Since IDH and TERTp mutations are identified in excised tissue after biopsy or surgery, there is a need to identify these genetic markers preoperatively for better treatment planning. Non-invasive detection of IDH and TERTp mutations would be beneficial for the optimization of diagnosis and treatment, including possible molecular-targeting therapy.

Magnetic resonance imaging (MRI) has become an important noninvasive method for the classification of gliomas. Dynamic susceptibility contrast MRI (DSC-MRI) is one of the standard perfusion-weighted MRI techniques widely used in clinical applications to provide information about tumor structure, functionality, and angiogenesis. Relative cerebral blood volume (rCBV) images derived from DSC-MRI have also been used to identify genetic subgroups in gliomas. Kickengereder et al. [9] reported an association between IDH mutation status and distinct angiogenesis that could be assessed on rCBV images. Moreover, Hakyemez et al. [10] and Sugahara et al. [11] identified histological grades and angiographic vascularities of gliomas and reported that rCBV images were useful in preoperative assessments. Tan et al. [12] attempted to investigate IDH mutations in astrocytomas based on rCBV values and reported that IDH-wt astrocytomas had higher rCBV values than IDH-mut astrocytomas. However, no studies have investigated the perfusion correlates of IDH along with TERTp mutations in gliomas.

Recently, with improvements in computational power, deep neural networks have become one of the most frequently used high-performance applications in medical image analysis. Several studies have proposed various convolutional neural network (CNN) architectures and radiomic models to successfully classify IDH and TERTp mutational status in public external or other internal datasets using various MRI sequences [13–16]. However, most CNN-based classification methods predict specific tumor subgroups without providing an explanation of how these mutations were determined or which tumor subsections played a role in decision-making. The attention mechanism in a deep learning architecture was first introduced as attention gates by Schlemper et al. [17] to improve the performance of medical image analysis and provide some insight into decision-making. A CNN model with an attention gate can learn the features within images without additional supervision and highlight salient features that are useful in a classification task. Another advantage of using attention gates in CNNs is that they can be easily adapted into any CNN architecture without high computational costs.

In this study, we propose a deep-learning approach with attention gates to classify IDH and TERTp mutation subgroups of gliomas using rCBV images. We hypothesized that a deep learning approach with attention gates may yield higher accuracies in the classification of these glioma mutational subgroups than classical machine learning utilizing rCBV images. Additionally, gradient-weighted class activation mapping (Grad-CAM) was employed to provide an explanation of which tumor parts played a role in decision-making during the classification process.

2. Materials and methods

2.1. Subjects

This retrospective study was approved by the Institutional Review Board, and a total of 337 pathologically confirmed glioma patients who underwent preoperative MRI at the Department of Neurosurgery, Acibadem University School of Medicine between 2014 and 2019 were initially included. Patients with a surgery or biopsy history (n = 49), imaging artifacts (n = 9), or missing data due to unknown IDH status (n = 20) or a lack of preoperative multiparametric imaging (n = 79) were excluded, along with the pediatric patients (n = 18). In the final cohort, 162 gliomas (100 males/62 females, mean age: 46.8 ± 14.7 years, range: 20–84 years) were included in this study (Fig. 1). The histopathological analysis was performed after surgical excision for all the tumors to determine the tumor subgroup according to the World Health Organization (WHO) 2021 Central Nervous System Tumor Classification Scheme by a pathologist with 13 years of experience (A.E.D.) [3] The TERTp and IDH mutations in the tissue were also determined by mini-sequencing [18] by the same pathologist and used as the ground truth reference. The final cohort included 88 glioblastoma-IDH wildtype, 74 IDH-mut (47 astrocytoma-IDH mutant and 27 oligodendroglioma-IDH mutant and 1p19q-codeleted), 64 TERTp-wt, and 74 TERTp-mut patients.

2.2. Image acquisition and data processing

The patients were scanned on a clinical 3 T MR scanner (Siemens Healthcare, Erlangen, Germany) using a 32-channel head coil before surgery. The brain tumor MRI protocol included pre- and post-contrast (gadolinium DTPA) T1-weighted TSE (TR = 532 ms, TE = 9.2 ms, voxel size = 0.69 mm × 0.69 mm × 3.6 mm), T2-weighted TSE (TR = 4250 ms, TE = 99 ms, voxel size = 0.22 mm × 0.22 mm × 3.6 mm), and T2*-weighted gradient-echo echo-planar imaging (EPI) DSC-MRI (TR = 1610 ms, TE = 30 ms voxel size = 1.80 mm × 1.80 mm × 6.5 mm). All images were pseudo-anonymized using an in-house MATLAB program. The rCBV maps were generated on the scanner console from the DSC-MRI by calculating the tissue tracer concentration divided by the arterial input function using the tissue 4D program (Siemens Healthcare, Erlangen, Germany). The program automatically determined the local arterial input function for each patient by considering all voxels throughout the time series, allowing the generation of rCBV images. The whole tumor masks were manually segmented on the T2-weighted (T2) MRI, and the enhancing tumor and necrosis masks were segmented on the contrast-enhanced T1-weighted (T1C) MRI. All tumor regions were validated by a radiologist with 31 years of experience (A.D.) regarding their pre and post-contrast T1-weighted, T2-weighted, and FLAIR images. The image intensities were normalized by subtracting the mean intensity followed by the division with standard deviation to deal with possible differences due to the scanner change and protocol modifications over time. Additionally, normal-appearing white matter (NAWM) regions of interest (ROI) were manually segmented on the contralateral side of the tumor for normalization purposes. The T1C and T2 MRI and their corresponding tumor masks were then co-registered onto the rCBV images using affine transformation with normalized mutual information as a cost function, 12 degrees of freedom, and nearest neighbor interpolation (Fig. 2). The segmentations were performed using Slicer3D [19], and the FMRIB Software Library (FSL) [20] and Advanced Normalization Tool (ANTs) [21] were used for the co-registrations.

Each pixel intensity of the rCBV images was normalized by the mean value of the corresponding NAWM ROI. The histograms of the rCBV data were assessed to compute the mean, median, standard deviation, skewness, and kurtosis parameters at the whole tumor area, excluding the necrosis for each patient, using an in-house script written in Python

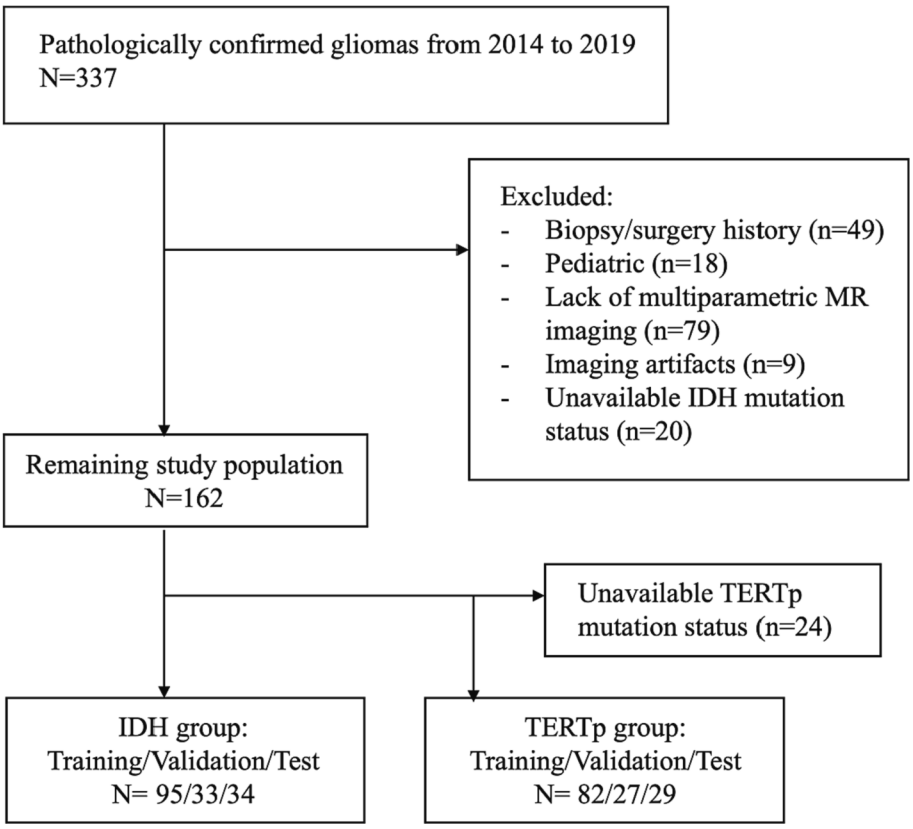

Fig. 1. Flow diagram of the study population exclusion criteria.

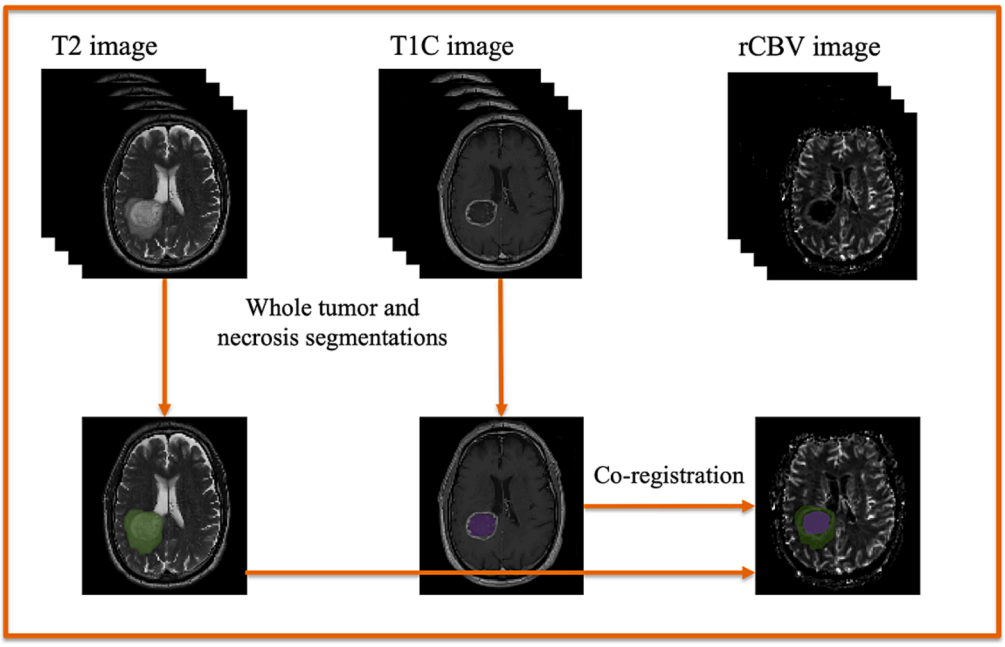

Fig. 2. The segmentation and co-registration example for a 67-year-old male grade 4 glioma patient. The green region represents the whole tumor, and the purple region represents the necrotic area. (For interpretation of the references to color in this figure legend, the reader is referred to the web version of this article.)

[22]. The differences in these parameters between the IDH or TERTp mutation subgroups, and TERTp-only versus "others" (IDH-mut-TERTp-mut, IDH-mut-TERTp-wt, and IDH-wt-TERTp-wt) were investigated using a Mann–Whitney *U* test with Bonferroni multiple comparison correction in IBM SPSS Statistics (IBM SPSS Statistics for MacOS, Version 27.0, Armonk, NY). Moreover, a Kruskal–Wallis test, followed by Dunn's tests, was used to analyze perfusion differences between astrocytoma, oligodendroglioma, and glioblastoma subgroups. The histogram parameters were also used as input features for several classical machine learning algorithms. Different supervised learning algorithms, including k-nearest neighbors, support vector machines (SVMs), decision trees, logistic regression, and linear discriminant analysis were evaluated with

an in-house program written in Python as a baseline model to classify IDH and TERTp mutations. All models were investigated with 10-fold cross-validation and the best-performed machine learning models were reported for each subgroup.

2.3. Deep learning approach

Two types of input images were created for deep learning. The first approach created an RGB image by placing the rCBV slice with the largest tumor area along with its previous and next slices into the three channels. The second approach created a multimodal image by placing the T1C, T2, and rCBV slices with the largest tumor area at the three RGB channels (Fig. 3). All images were automatically cropped to a rectangular bounding box, including the tumor area, and resized to 128 × 128. The data cohort was then split into training, validation, and held-out test sets by a 60:60:20 ratio. Afterwards, pre-trained network models, including ResNet50 [23] and VGG16 [24], were utilized to determine the best-performing network architecture for the classification tasks using Python with Keras [25] and Tensorflow [26] libraries. The use of pretrained networks allowed for knowledge transfer for image classification while they prevented overfitting on our relatively small dataset.

In the final approach, two attention gates were added—after stages 2 and 3 of the ResNet50 architecture and after stages 3 and 4 of the VGG16 architecture—and their outputs were flattened and aggregated (Fig. 4). Since the dataset is relatively small, data augmentation techniques were incorporated into the process to minimize overfitting. The ImageDataGenerator class of Keras API [25] was utilized for data augmentation purposes. The ImageDataGenerator generates batches of image data and ensures that the model receives different variations (random rotations, width and height shifts, shear, zoom, and vertical and horizontal flips) of the images at each epoch, which helps prevent overfitting. We augment the data only in the training set to prevent data leakage.

Additionally, the loss and accuracy curves were analyzed to assess if the models were overfitting. Finally, the best-performing models were selected and tested on the held-out test set to report accuracy, confidence intervals, specificity, sensitivity, no information rate (NIR), and the area under the receiver operating characteristic curve (AUC) for the classification tasks. NIR represents the accuracy that could be achieved by a model by predicting the most frequent class for all instances in a classification problem. The accuracy of the models was compared with that of NIR by using a binomial one-sided test. [27] The area under the receiver operating characteristic curve (AUC) for the deep learning models was also investigated (Table 5).

The Checklist for Artificial Intelligence in Medical Imaging (CLAIM) [28] was filled and included as a supplementary document (Appendix A) for providing more details of the artificial intelligence (AI) approach in this study.

2.4. Hyperparameter optimization

To maximize the validation accuracy of the models, a detailed hyperparameter search was carried out on the most impactful features using the Weights & Biases [29] platform. The sets of basic model parameters, such as learning rate and batch size, were examined, and the effect of adding dropout layers for further regularization was investigated. Stochastic gradient descent, root mean squared propagation and adaptive moment estimation optimization algorithms were used to find the best-performing optimization method. Lastly, the grid search method [30] was applied to find the best combination of all features.

2.5. Explainable AI

Since deep neural networks consist of many layers and connections, and how these layers and connections decide the outcome is not very clear, they are often considered black box models. Recently, explainable AI has gained popularity to shed light on the decision-making process of deep learning models. A Grad-CAM, which creates visual explanations for any CNN-based model, was employed in this study [31]. With the

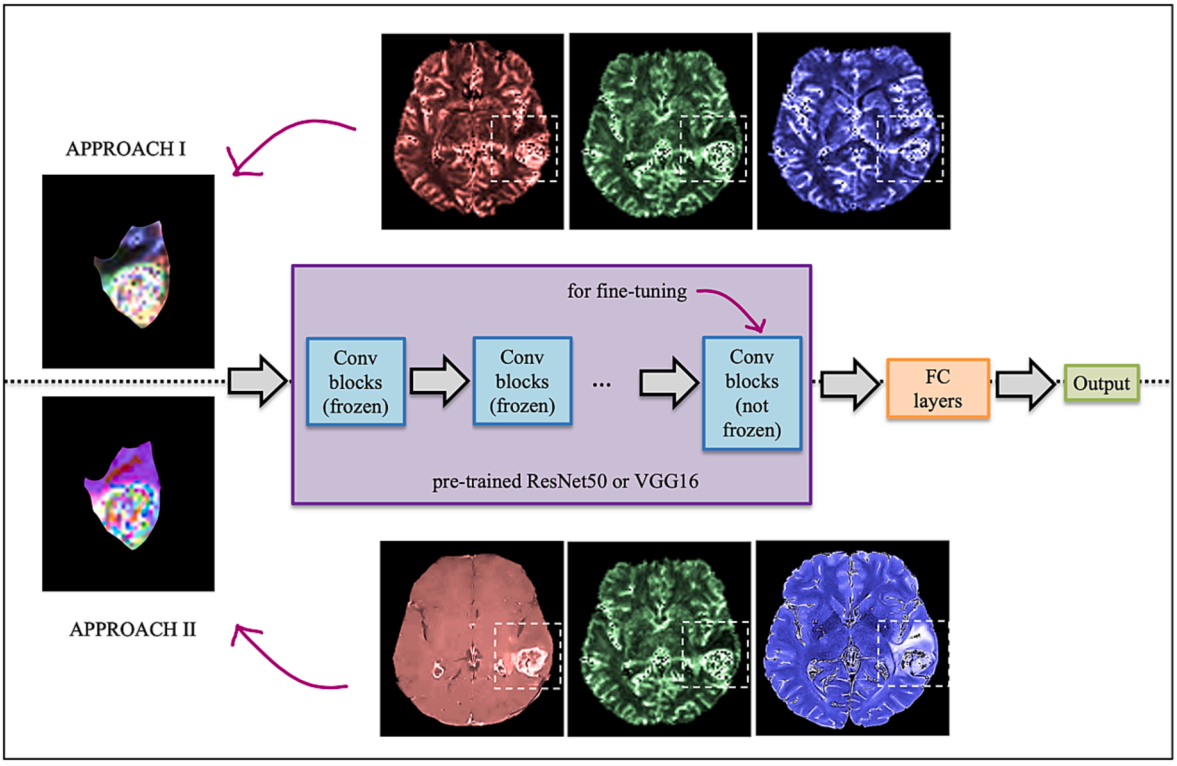

Fig. 3. Approach I. RGB images containing three consecutive rCBV slices were used as inputs, approach II. RGB images containing three different modalities (T1C, T2, and rCBV) were used as inputs for the pre-trained networks.

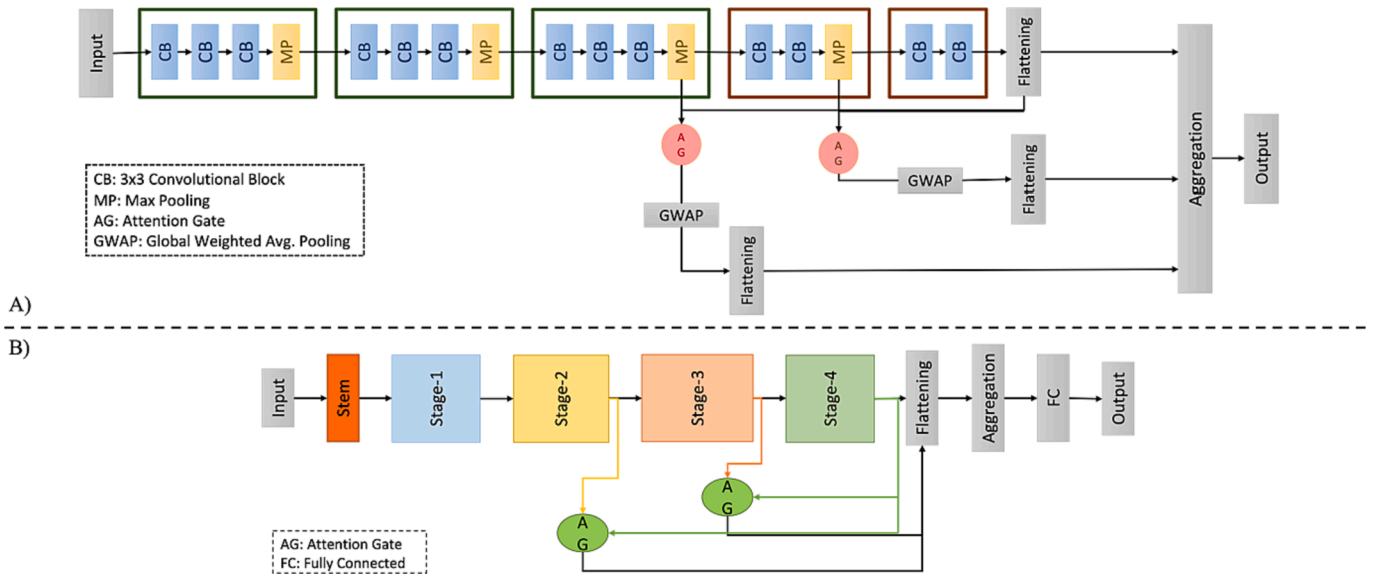

Fig. 4. Proposed models: Two attention gates were added after (A) stages 3 and 4 of VGG16 architecture, and (B) stages 2 and 3 of the ResNet50 structure and aggregated together after the flattening layer.

visualization of salient features, the effect of signal intensities at different tumor parts on genetic subgroups prediction was investigated.

3. Results

3.1. Statistical analysis

The clinical characteristics of the patient cohort according to the WHO 2021 brain tumor classification are reported in Table 1. In the IDH-mut subgroup, the majority of the tumors were astrocytomas (63.5 %), while the IDH-wt subgroup included only glioblastomas per the new guidelines. In the TERTp-mut group, there was only one astrocytoma (1.4 %), while the majority were glioblastomas (64.8 %). By contrast, in the TERTp-wt subgroup, there were only two oligodendrogliomas (3.1 %), and the majority of the tumors were astrocytomas (65.6 %). In the TERTp-only subgroup, all patients were glioblastomas, and in the "others" group (IDH-mut-TERTp-mut, IDH-mut-TERTp-wt, and IDH-wt-TERTp-wt), the majority were astrocytomas (49.5 %). Overall, 87 out of 162 patients (17 IDH-mut and 70 IDH-wt; 8 astrocytomas, 9 oligodendrogliomas, and 70 glioblastomas) had contrast enhancement and necrosis in their T1C images.

A Mann-Whitney *U* test indicated that IDH-wt gliomas had a higher median ($p = 0.007$), mean ($p < 0.001$), and standard deviation ($p < 0.001$), and lower skewness ($p < 0.001$) and kurtosis ($p < 0.001$) values than IDH-mut patients in the tumor region (Table 2). By contrast, TERTp-mut gliomas had higher median ($p = 0.001$), and lower skewness ($p = 0.001$) values than TERTp-wt patients. Similarly, TERTp-only glioma patients had higher median ($p = 0.010$), and lower skewness ($p <$

Table 2
The differences of several histogram properties of IDH-mut versus IDH-wt, TERTp-mut versus TERTp-wt, and TERTp-only versus other subgroups.

	IDH-mut (n = 74) mean ± std	IDH-wt (n = 88) mean ± std	p-value
Median	2.05 ± 1.04	2.83 ± 1.94	0.007*
Mean	2.64 ± 1.18	3.67 ± 2.12	<0.001*
Standard Deviation	2.04 ± 0.88	2.86 ± 1.83	<0.001*
Skewness	2.27 ± 0.69	1.74 ± 0.75	<0.001*
Kurtosis	11.09 ± 5.25	7.72 ± 4.60	<0.001*
	TERTp-mut (n = 74) mean ± std	**TERTp-wt (n = 64) mean ± std**	
Median	2.82 ± 1.82	2.01 ± 1.07	0.001*
Mean	3.53 ± 2.15	2.73 ± 1.28	0.015
Standard deviation	2.54 ± 1.87	2.27 ± 1.10	0.522
Skewness	1.79 ± 0.75	2.20 ± 0.74	0.001*
Kurtosis	8.34 ± 4.92	10.36 ± 5.42	0.012
	TERTp-only (n = 48) mean ± std	**Others (n = 95) mean ± std**	
Median	2.98 ± 2.06	2.15 ± 1.13	0.010*
Mean	3.78 ± 2.45	2.81 ± 1.30	0.013
Standard deviation	2.78 ± 2.20	2.22 ± 1.03	0.195
Skewness	1.70 ± 0.80	2.15 ± 0.72	<0.001*
Kurtosis	7.82 ± 5.60	10.28 ± 5.29	0.001*
			*p < 0.05

Table 1
The clinical characteristics of the patient cohort of this study.

	IDH-mut (n = 74)	IDH-wt (n = 88)	TERTp-mut (n = 74)	TERTp-wt (n = 64)	TERTp-only (n = 48)	Others (n = 95)
Age	38.85 ± 12.58	53.55 ± 12.89	51.73 ± 13.34	39.11 ± 13.84	57.23 ± 11.52	40.13 ± 13.00
Sex (%)						
- Female	35 (47.3 %)	27 (30.7 %)	26 (35.1 %)	31 (48.4 %)	17 (35.4 %)	40 (42.1 %)
- Male	39 (52.7 %)	61 (69.3 %)	48 (64.9 %)	33 (51.6 %)	31 (64.6 %)	55 (57.9 %)
Histopathological subgroup						
- Astrocytoma	47 (63.5 %)	–	1 (1.4 %)	42 (65.6 %)	–	47 (49.5 %)
- Oligodendroglioma	27 (36.5 %)	–	25 (33.8 %)	2 (3.1 %)	–	27 (28.4 %)
- Glioblastoma	–	88 (100 %)	48 (64.8 %)	20 (31.3 %)	48 (100 %)	21 (22.1 %)

The histopathological subgroup is in accordance with the revised WHO 2021 brain tumor classification.

0.001) and kurtosis (p = 0.001) values than the other gliomas. Further, there were several statistically significant differences between the three histopathological subgroups (Table 3). Glioblastomas had a higher median (p = 0.001), mean (p < 0.001), and standard deviation (p = 0.001) and lower skewness (p < 0.001) and kurtosis (p < 0.001) than astrocytomas. Moreover, astrocytomas had lower median values (p = 0.029) than oligodendrogliomas.

3.2. Classical machine learning

Using classical machine learning algorithms, the IDH mutation subgroup was classified with 83.3 % accuracy (95 % CI [0.606, 1.0], NIR = 0.55 (p < 0.05), 82.9 % specificity, and 83.8 % sensitivity) using linear discriminant analysis, the TERTp subgroup was classified with 68.1 % accuracy (95 % CI [0.437, 0.938], NIR = 0.54 (p = 0.30), 67.2 % specificity and 68.9 % sensitivity) using random forest, and the TERTp-only versus others was classified with 76.9 % accuracy (95 % CI [0.515, 1.0], NIR = 0.65 (p = 0.42), 85.2 % specificity and 60.4 % sensitivity) using SVMs (Table 4). Only the accuracy for the classification of IDH was statistically significantly higher than NIR (p < 0.05) using the classical machine learning models.

3.3. Deep learning approach

For the first deep-learning approach with pretrained networks using the three consecutive slices of the rCBV images, the best-performing model achieved 81 % accuracy on the test set (95 % CI [0.65, 0.93], NIR = 0.55 (p < 0.01), specificity = 0.79, sensitivity = 0.83) for the classification of the IDH mutational subgroup, 62 % accuracy (95 % CI [0.42, 0.80], NIR = 0.62 (p = 0.71), specificity = 0.57, sensitivity = 0.67) for the classification of the TERTp mutational subgroup and 83 % accuracy (95 % CI [0.65, 0.93], NIR = 0.61 (p < 0.01), specificity = 0.87, sensitivity = 0.75) for that of the TERTp-only versus others. However, for the three modality images, the classification accuracy reached up to 80 % (95 % CI [0.63, 0.93], NIR = 0.58 (p < 0.01), specificity = 0.79, sensitivity = 0.82) for the IDH subgroup, 65 % (95 % CI [0.45, 0.88], NIR = 0.55 (p = 0.13), specificity = 0.82, sensitivity = 0.55) for the TERTp subgroup, and 80 % (95 % CI [0.63, 0.93], NIR = 0.55 (p < 0.01), specificity = 0.71, sensitivity = 0.91) for the TERTp-only versus the others. In the final approach, attention gates were added to the both ResNet50 and VGG16 structures, and the models achieved 81 % accuracy (95 % CI [0.65, 0.94], NIR = 0.55 (p < 0.01), specificity = 0.86, sensitivity = 0.75) for the classification of the IDH subgroup, 55 % (95 % CI [0.39, 0.76], NIR = 0.62 (p = 0.72), specificity = 0.71, sensitivity = 0.40) for the TERTp subgroup, and 83 % accuracy (95 % CI [0.65, 0.93], NIR = 0.61 (p < 0.01), specificity = 0.93, sensitivity = 0.63) for the TERTp-only versus the others using the three consecutive rCBV slices. Using the same attention-boosted structures with multimodality RGB images, the models achieved 88 % accuracy (95 % CI [0.71, 0.96], NIR = 0.58 (p < 0.01), specificity = 0.86, sensitivity = 0.91) for the classification of the IDH subgroup, 70 % accuracy (95 % CI [0.46, 0.88], NIR = 0.55 (p = 0.13), specificity = 0.67, sensitivity = 0.73) for the TERTp subgroup and 84 % accuracy (95 % CI [0.66, 0.95], NIR = 0.55 (p < 0.01), specificity = 0.86, sensitivity = 0.82) for the TERTp-only versus others classification. The accuracies achieved in the training, validation, and test sets along with the AUCs are reported in Table 5. Although TERTp mutational subgroup classification was not better than NIR, the classification accuracies of both IDH and TERTp-only subgroups were statistically significantly higher than NIR (p < 0.05). Fig. 5 illustrates the accuracy and loss curves for the best-performed models for the classification of IDH mutational status (A, B), TERTp mutational status (C, D), and TERTp-only identification (E, F). For both the IDH and TERTp-only subgroups, the plots of training losses decreased to 0.55 after 20 epochs. The plots of validation losses also decreased to a stable point after 30 epochs and had a small gap with the training losses. The accuracy curves also plateaued around 80–85 % accuracy after 20 epochs and showed a good fit for the models. TERTp mutational group also showed similar characteristics regarding validation and training losses, however, the maximum accuracy could not exceed 70 %.

Fig. 6 shows the heatmaps obtained from the Grad-CAM analysis, which depicts the regions the network focused on within the tumor, along with the T1C, rCBV, and T2 images and the RGB image created from these three modalities at the corresponding slice for an IDH-wt and a TERTp-only patient examples. The heatmaps represented the salient features, where the red regions were the most important pixels for the CNN model. Based on this approach, most of the higher-importance features were located in the edema part, therefore the CNN model primarily focused on the edema region for identifying the TERTp-only mutation in the example. Conversely, these features were located at the tumor core and necrosis area in the case of the IDH-mut example, therefore the model predominantly concentrated on the tumor core

Table 3
The differences in several histogram properties of astrocytomas (ASTRO), oligodendrogliomas (OLIGO), and glioblastomas (GBM) with adjusted p values after multi-comparison correction.

	ASTRO (n = 47) mean ± std	OLIGO (n = 27) mean ± std	GBM (n = 88) mean ± std	p-value
Median	1.79 ± 0.81	2.51 ± 1.24	2.83 ± 1.94	0.001*
Mean	2.41 ± 0.98	3.06 ± 1.40	3.67 ± 2.20	<0.001*
Standard deviation	1.99 ± 0.88	2.13 ± 0.90	2.86 ± 1.83	0.001*
Skewness	2.43 ± 0.68	1.991 ± 0.62	1.74 ± 0.75	<0.001*
Kurtosis	12.03 ± 5.41	9.475 ± 4.61	7.72 ± 4.60	<0.001*
Post hoc results	**ASTRO vs. OLIGO**	**ASTRO vs. GBM**	**OLIGO vs. GBM**	
Median	0.029*	0.001*	0.908	
Mean	0.117	<0.001*	0.847	
Standard deviation	0.479	0.002*	0.121	
Skewness	0.064	<0.001*	0.199	
Kurtosis	0.207	<0.001*	0.091	
				*p < 0.05

Table 4
Machine learning-based classification results for mean, median, standard deviation, skewness, and kurtosis values derived from rCBV maps.

Subjects	Accuracy (%)	Specificity (%)	Sensitivity (%)
IDH-mut vs. IDH-wt	83.3	82.9	83.8
TERTp-mut vs. TERTp-wt	68.1	67.2	68.9
TERTp-only vs. others	76.9	85.2	60.4

Table 5
Classification results for all deep learning approaches.

Approach	Group	Training Accuracy	Validation Accuracy	Test Accuracy	AUC
rCBV images	IDH	0.88	0.83	0.81	0.82
	TERTp	0.81	0.77	0.62	0.61
	TERTp-only	0.88	0.85	0.83	0.81
rCBV + anatomical images	IDH	0.86	0.80	0.80	0.80
	TERTp	0.60	0.77	0.65	0.67
	TERTp-only	0.85	0.71	0.80	0.82
rCBV images with attention gates	IDH	0.86	0.82	0.81	0.81
	TERTp	0.73	0.69	0.55	0.59
	TERTp-only	0.85	0.80	0.83	0.81
rCBV + anatomical images with attention gates	IDH	0.91	0.87	0.88	0.89
	TERTp	0.78	0.72	0.70	0.70
	TERTp-only	0.87	0.85	0.84	0.85

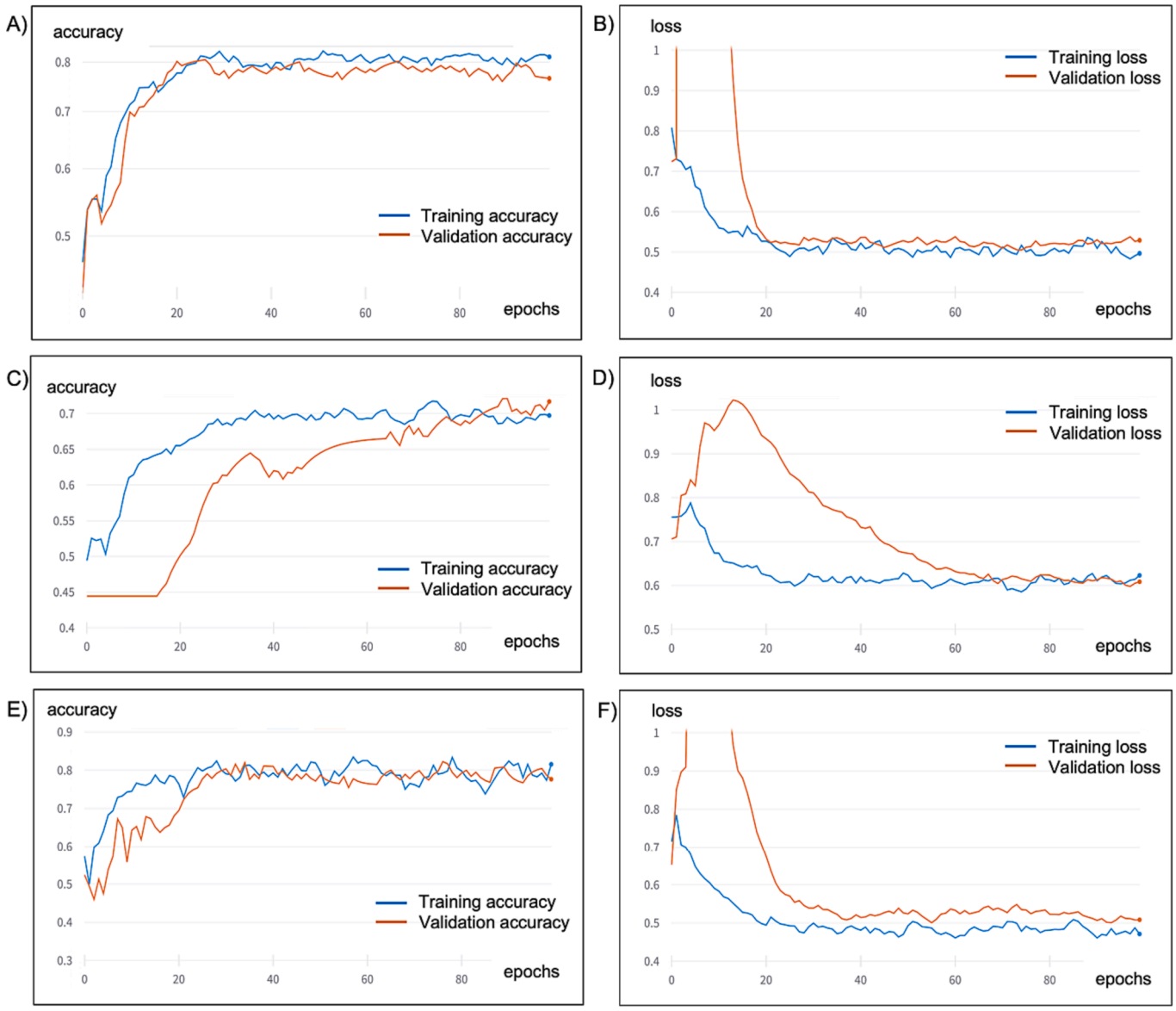

Fig. 5. Training and validation accuracy and loss curves for the attention-boosted model in different subgroups: IDH mutational subgroup (A, B), TERTp mutational subgroup (C, D), and TERTp-only subgroup (E, F).

region.

4. Discussion

This study demonstrated that incorporating rCBV images obtained from DSC-MRI into a deep learning model provides high-performance differentiation between glioma subgroups based on IDH and TERTp mutations. To our knowledge, this is the first study to classify both IDH and TERTp mutations in diffuse gliomas using rCBV images with deep learning applications. Our results indicated that IDH mutational status was successfully identified with 88 % accuracy based on a combination of anatomical images with rCBV images. Although our models were not as successful in the identification of the TERTp mutational status in gliomas, TERTp-only gliomas were classified with 84 % accuracy. Moreover, the inclusion of an attention scheme in the deep learning model significantly improved the noninvasive identification of the IDH and TERTp mutational status of gliomas based on the rCBV images. GradCAM approach also illustrated the regions where the deep learning models focused on within the tumor.

MRI techniques have been successful in classifying IDH mutational subgroups in gliomas [32]. Multiple studies have utilized DSC-MRI to focus on distinguishing the molecular glioma subgroups, as it provides valuable information about tumor vascularization and biology [33]. While TERTp mutation remains a significant predictor of prognosis in gliomas, its role appears to differ across various glioma subgroups [34]. TERTp mutation has been associated with a favorable prognosis in oligodendrogliomas characterized by IDH mutations and 1p19q codeletion; however, it is a marker of poor prognosis in the IDH-wt gliomas specifically the TERTp-only subgroup [35]. Furthermore, the WHO 2021 glioma classification scheme demonstrates that IDH and TERTp mutations can differentiate the three glioma subgroups. The astrocytoma (-IDH-mut) group is classified based on IDH mutation without TERTp mutation, the oligodendroglioma (-IDH-mut and 1p/19q-codel) group is classified with both mutations, and the glioblastoma (-IDH-wt) group is categorized without IDH mutation [3]. Thus, predicting the TERTp mutation was one of the key objectives of this study, and the utilization of deep learning models based on rCBV images yielded promising classification accuracies for detecting IDH-mut and TERTp-only subgroups of gliomas.

There have been several studies that identified different molecular

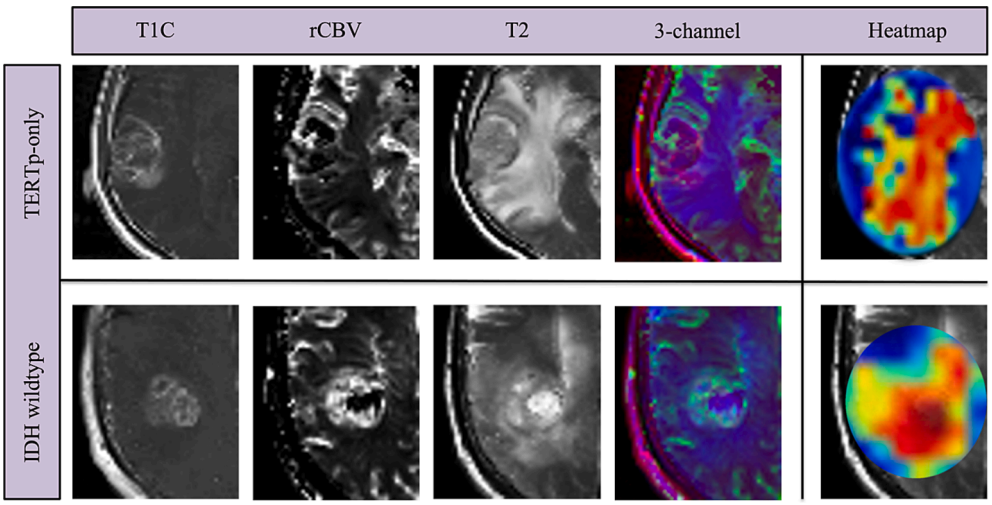

Fig. 6. The T1C, T2, and rCBV images, along with the RGB images that had these three modalities at their channels, and the heatmaps of their visual saliency in our proposed model for an IDH-wt and a TERTp-only patient that were correctly classified.

subgroups of gliomas based on MR perfusion metrics [36–39]. Leu et al. [36] demonstrated higher rCBV values in the IDH-wt group, although the difference was not statistically significant. They also reported higher rCBV values in astrocytomas than in oligodendrogliomas, which was not consistent with our findings. However, Leu et al.'s study only had low-grade gliomas based on WHO 2007 and 2016 classification schemes, which might have resulted in this discrepancy. Additionally, Arzanforoosh et al. [37] reported the lowest rCBV values in astrocytomas and the highest rCBV values in oligodendrogliomas rather than in glioblastomas, since they only investigated non-enhancing gliomas. On the other hand, Pruis et al. [38] reported higher rCBV values in glioblastomas, lower rCBV values in oligodendrogliomas, and the lowest rCBV values in astrocytomas in a cohort of non-enhancing gliomas, which was similar to our findings. Moreover, Wang et al. [39] showed that TERTp-mut gliomas had higher rCBV values than TERTp-wt gliomas using computed tomography (CT) scans. These findings are in line with our findings of highest rCBV in IDH-wt tumors, lower rCBV in oligodendrogliomas, and lowest rCBV in astrocytomas. Additionally, we showed that IDH-mut gliomas displayed lower rCBV values compared to TERTp-only gliomas. These results shed light to the underlying tumor biology of IDH-wt gliomas with increased vascularity and thus increased blood volume.

Deep learning methods, especially CNN architectures, have been utilized for the classification of glioma subgroups [40]. Several studies have investigated hybrid models combining deep learning approaches and radiomics to predict the molecular subgroups of gliomas [14,41,42]. Choi et al. [14] proposed an architecture that integrates radiomics and CNN image features for predicting IDH mutational status in diffuse gliomas using anatomical MRI. Fukuma et al. [41] also developed hybrid models that combine deep learning and radiomics to predict the IDH mutation status of low-grade gliomas. Another study presented a method using a multi-task CNN neural structural MRI to predict the IDH mutation and 1p19q-codeletion status and grade of gliomas while also providing tumor segmentation [42]. Additional studies have incorporated other advanced MRI methods, such as MR spectroscopy (MRS) and diffusion MRI, to classify glioma subgroups [8,15,16,43,44]. Classical machine learning models were used to differentiate IDH-mutational subgroups with over 85 % accuracy based on lower myoinositol and NAA, and higher glycine, glutathione (GSH), choline (Cho), and glutamate-glutamine complex (Glx); and TERTp-only from others with 81 % accuracy based on higher GSH, Cho and Glx using MRS [8]. The results of this MRS study identified IDH-wt and TERTp-only groups as having more aggressive metabolic profiles, which are consistent with our results. Additionally, Calabrese et al. [43] utilized a hybrid deep learning approach with multimodal MRI, including diffusion and perfusion images, to predict genetic biomarkers such as IDH and TERTp mutations in WHO grade 4 astrocytomas and glioblastomas. Moreover, Cluceru et al. [15], and Ma et al. [44] combined diffusion-weighted MRI with anatomical MRI to predict IDH mutational and 1p19q-codeletion status of all subgroups of gliomas. Pasquini et al. [16], also utilized diffusion and perfusion metrics to classify IDH mutations in glioblastomas. However, unlike these studies, our patient cohort encompassed all WHO tumor grades and subgroups for diffuse gliomas with varying IDH and TERTp mutational status using multimodal MRI. The concept of using transfer learning on RGB color images generated from grayscale anatomical MRI combined with diffusion-weighted imaging was first introduced by Cluceru et al. [15]. We adopted their approach by creating an RGB image with anatomical and rCBV images placed in different channels. Additionally, we incorporated three consecutive rCBV slices into the RGB channels to compare the performance of the two approaches. Our findings highlight the importance of incorporating more advanced MRI sequences in deep learning models for a better classification of glioma mutational subgroups.

Recently, an attention mechanism has been proposed in the context of medical image analysis. These mechanisms enable models to automatically learn and focus on specific target structures within the images. By incorporating attention gates into CNN structures, models can effectively suppress irrelevant regions and emphasize salient features in the input images. This flexibility has led to numerous studies exploring the use of attention mechanisms to learn target features in images without the need for supervision. Oktay et al. [45] applied an attention U-Net model to an abdominal CT dataset with the goal of pancreatic segmentation. Comparing their model to a standard 3D U-Net, they observed that the attention gates not only improved the accuracy of predictions but also maintained computational efficiency. Schlemper et al. [17] applied an attention U-Net model to real-time automated scan plane detection for fetal ultrasound screening. By incorporating self-gated soft-attention mechanisms, they demonstrated that the addition of attention gates can effectively enhance object localization and overall performance, particularly when the base network has a high capacity. Similarly, attention mechanisms have been employed in other studies focusing on tumor segmentation and survival prediction in gliomas [46,47]. However, to the best of our knowledge, there is a lack of research for the classification of genetic mutations in gliomas utilizing attention mechanisms. According to our results, incorporating attention gates into our models improved classification accuracies without retraining or the necessity of architectural changes. Since an attention mechanism allows deep learning models to focus on different parts of the tumor with varying degrees of importance, it can highlight the

important regions that are most relevant for the classification of glioma mutational subgroups. Therefore, the performance of the models could be improved with an attention mechanism. Although our accuracies were similar to the existing studies in the literature, there is a potential for improved performance by using a larger dataset.

Our study had several limitations. Firstly, it is important to note that this study was retrospective, and the number of subjects may be considered relatively small for deep learning applications. However, it is worth highlighting that our study included one of the largest glioma datasets that have been reported so far, containing both anatomical MRI and DSC-MRI with histopathological data. It is important to note that due to the unavailability of DSC-MRI data in public datasets, we were unable to externally validate our models for evaluating their generalizability. One limitation of using deep learning models is their black-box structure which doesn't provide a clear understanding of the decision-making process. To provide some insights into the model's inner workings, we employed the GradCAM algorithm. GradCAM is an explainable AI algorithm that provides salient features in the form of a heatmap, which can be considered a map of where the model focuses on the image for decision-making to decide its outcome. Lastly, we acknowledge that the inclusion of other advanced imaging techniques, such as diffusion MRI, could potentially enhance classification accuracies. Therefore, in our future studies, we aim to investigate the impact of incorporating additional MRI modalities into attention-boosted deep learning models for the classification of genetic mutations in gliomas.

In conclusion, our study demonstrated that deep learning-based classification of IDH mutational and TERTp-only subsets of gliomas using rCBV images obtained from DSC-MRI in combination with anatomical MRI yielded high accuracy rates. The incorporation of attention gates highlighted the significance of different tumor components in the preoperative molecular classification of gliomas. The proposed deep learning-based method might have the potential to assist clinicians in identifying IDH mutation and TERTp-only subsets of gliomas at the pre-surgery point and could potentially aid in improving treatment planning and patient outcomes.

CRediT authorship contribution statement

Buse Buz-Yalug: Data curation, Methodology, Software, Formal analysis, Writing – original draft. **Gulce Turhan:** Methodology, Software, Writing – review & editing. **Ayse Irem Cetin:** Methodology, Software, Writing – review & editing. **Sukru Samet Dindar:** Methodology, Software, Writing – review & editing. **Ayca Ersen Danyeli:** Supervision, Conceptualization, Investigation, Resources, Writing - review & editing. **Cengiz Yakicier:** Investigation, Resources, Writing – review & editing. **M. Necmettin Pamir:** Investigation, Resources, Writing – review & editing. **Koray Ozduman:** Supervision, Conceptualization, Investigation, Resources, Writing – review & editing. **Alp Dincer:** Supervision, Conceptualization, Investigation, Resources, Writing – review & editing. **Esin Ozturk-Isik:** Conceptualization, Supervision, Investigation, Writing – review & editing.

Declaration of competing interest

The authors declare that they have no known competing financial interests or personal relationships that could have appeared to influence the work reported in this paper.

Acknowledgments

Grant support: This study was supported by the Scientific and Technological Research Council of Turkey (TUBITAK) 1003 grant (216S432).

Appendix A. Supplementary material

Supplementary data to this article can be found online at https://doi.org/10.1016/j.ejrad.2023.111257.

References

[1] Q.T. Ostrom, G. Cioffi, K. Waite, et al., CBTRUS statistical report: primary brain and other central nervous system tumors diagnosed in the United States in 2014–2018, Neuro Oncol. 23 (12 Suppl. 2) (2021) iii1–iii105, https://doi.org/10.1093/neuonc/noab200. Epub 2021/10/06.
[2] J.E. Eckel-Passow, D.H. Lachance, A.M. Molinaro, et al., Glioma groups based on 1p/19q, IDH, and TERT promoter mutations in tumors, N. Engl. J. Med. 372 (26) (2015) 2499–2508, https://doi.org/10.1056/NEJMoa1407279.
[3] D.N. Louis, A. Perry, P. Wesseling, et al., The 2021 WHO classification of tumors of the central nervous system: a summary, Neuro Oncol. 23 (8) (2021) 1231–1251, https://doi.org/10.1093/neuonc/noab106. Epub 2021/06/30.
[4] M.J. Riemenschneider, J.W. Jeuken, P. Wesseling, G. Reifenberger, Molecular diagnostics of gliomas: state of the art, Acta Neuropathol. 120 (5) (2010) 567–584, https://doi.org/10.1007/s00401-010-0736-4.
[5] H. Yan, D.W. Parsons, G. Jin, et al., IDH1 and IDH2 mutations in gliomas, N. Engl. J. Med. 360 (8) (2009) 765–773, https://doi.org/10.1056/NEJMoa0808710.
[6] C.G.A.R. Network, Comprehensive, integrative genomic analysis of diffuse lower-grade gliomas, N. Engl. J. Med. 372 (26) (2015) 2481–2498, https://doi.org/10.1056/NEJMoa1402121.
[7] P.J. Killela, C.J. Pirozzi, P. Healy, et al., Mutations in IDH1, IDH2, and in the TERT promoter define clinically distinct subgroups of adult malignant gliomas, Oncotarget 5 (6) (2014) 1515, https://doi.org/10.18632/oncotarget.1765.
[8] E. Ozturk-Isik, S. Cengiz, A. Ozcan, et al., Identification of IDH and TERTp mutation status using (1) H-MRS in 112 hemispheric diffuse gliomas, J. Magn. Reson. Imaging 51 (6) (2020) 1799–1809, https://doi.org/10.1002/jmri.26964. Epub 2019/10/31.
[9] P. Kickingereder, F. Sahm, A. Radbruch, et al., IDH mutation status is associated with a distinct hypoxia/angiogenesis transcriptome signature which is non-invasively predictable with rCBV imaging in human glioma, Sci. Rep. 5 (1) (2015), 16238, https://doi.org/10.1038/srep16238.
[10] B. Hakyemez, C. Erdogan, I. Ercan, et al., High-grade and low-grade gliomas: differentiation by using perfusion MR imaging, Clin. Radiol. 60 (4) (2005) 493–502, https://doi.org/10.1016/j.crad.2004.09.009.
[11] T. Sugahara, Y. Korogi, M. Kochi, et al., Correlation of MR imaging-determined cerebral blood volume maps with histologic and angiographic determination of vascularity of gliomas, AJR Am. J. Roentgenol. 171 (6) (1998) 1479–1486, https://doi.org/10.2214/ajr.171.6.9843274. Epub 1998/12/08.
[12] W. Tan, J. Xiong, W. Huang, et al., Noninvasively detecting Isocitrate dehydrogenase 1 gene status in astrocytoma by dynamic susceptibility contrast MRI, J. Magn. Reson. Imaging 45 (2) (2017) 492–499, https://doi.org/10.1002/jmri.25358. Epub 2016/07/02.
[13] C.G. Bangalore Yogananda, B.R. Shah, M. Vejdani-Jahromi, et al., A novel fully automated MRI-based deep-learning method for classification of IDH mutation status in brain gliomas, Neuro Oncol. 22 (3) (2019) 402–411, https://doi.org/10.1093/neuonc/noz199.
[14] Y.S. Choi, S. Bae, J.H. Chang, et al., Fully automated hybrid approach to predict the IDH mutation status of gliomas via deep learning and radiomics, Neuro Oncol. 23 (2) (2020) 304–313, https://doi.org/10.1093/neuonc/noaa177.
[15] J. Cluceru, Y. Interian, J.J. Phillips, et al., Improving the noninvasive classification of glioma genetic subtype with deep learning and diffusion-weighted imaging, Neuro Oncol. 24 (4) (2022) 639–652, https://doi.org/10.1093/neuonc/noab238. Epub 2021/10/16.
[16] L. Pasquini, A. Napolitano, E. Tagliente, et al., Deep learning can differentiate IDH-mutant from IDH-wild GBM, J. Pers. Med. 11 (4) (2021), https://doi.org/10.3390/jpm11040290. Epub 2021/05/01.
[17] J. Schlemper, O. Oktay, M. Schaap, et al., Attention gated networks: learning to leverage salient regions in medical images, Med. Image Anal. 53 (2019) 197–207, https://doi.org/10.1016/j.media.2019.01.012. Epub 2019/02/26.
[18] C.B. Akyerli, Ş. Yüksel, Ö. Can, et al., Use of telomerase promoter mutations to mark specific molecular subsets with reciprocal clinical behavior in IDH mutant and IDH wild-type diffuse gliomas, J. Neurosurg. 128 (4) (2018) 1102–1114, https://doi.org/10.3171/2016.11.JNS16973.
[19] A. Fedorov, R. Beichel, J. Kalpathy-Cramer, et al., 3D Slicer as an image computing platform for the Quantitative Imaging Network, Magn. Reson. Imaging 30 (9) (2012) 1323–1341, https://doi.org/10.1016/j.mri.2012.05.001.
[20] M. Jenkinson, C.F. Beckmann, T.E. Behrens, et al., Fsl. Neuroimage 62 (2) (2012) 782–790, https://doi.org/10.1016/j.neuroimage.2011.09.015.
[21] B.B. Avants, N.J. Tustison, G. Song, et al., A reproducible evaluation of ANTs similarity metric performance in brain image registration, Neuroimage 54 (3) (2011) 2033–2044, https://doi.org/10.1016/j.neuroimage.2010.09.025.
[22] G. Van Rossum, F.L. Drake Jr, Python tutorial, Centrum voor Wiskunde en Informatica Amsterdam, The Netherlands, 1995.
[23] K. He, X. Zhang, S. Ren, J. Sun, Deep residual learning for image recognition, in: Proceedings of the IEEE Conference on Computer Vision and Pattern Recognition (CVPR), 2016, https://doi.org/10.1109/CVPR.2016.90.
[24] K. Simonyan, A. Zisserman, Very deep convolutional networks for large-scale image recognition, arXiv preprint arXiv:14091556, 2014, doi: 10.48550/arXiv.1409.1556.

[25] Chollet Fao, Keras, 2015, Available from: https://keras.io.
[26] M. Abadi, A. Agarwal, P. Barham, et al., TensorFlow: Large-scale machine learning on heterogeneous systems, 2015, Available from: https://www.tensorflow.org.
[27] M. Bicego, A. Mensi, Null/No Information Rate (NIR): a statistical test to assess if a classification accuracy is significant for a given problem, arXiv preprint arXiv: 230606140, 2023.
[28] J. Mongan, L. Moy, C.E. Kahn Jr, Checklist for artificial intelligence in medical imaging (CLAIM): a guide for authors and reviewers, Radiol. Artif. Intell. (2020), e200029, https://doi.org/10.1148/ryai.2020200029.
[29] L. Biewald, Experiment tracking with weights and biases, Software available from wandb.com. 2020;2:233.
[30] S.M. LaValle, M.S. Branicky, S.R. Lindemann, On the relationship between classical grid search and probabilistic roadmaps, Int. J. Rob. Res. 23 (7–8) (2004) 673–692, https://doi.org/10.1177/0278364904045481.
[31] R.R. Selvaraju, M. Cogswell, A. Das, et al., Grad-cam: visual explanations from deep networks via gradient-based localization, in: Proceedings of the IEEE International Conference on Computer Vision (ICCV), 2017, https://doi.org/10.1109/ICCV.2017.74.
[32] C.H. Suh, H.S. Kim, S.C. Jung, et al., Imaging prediction of isocitrate dehydrogenase (IDH) mutation in patients with glioma: a systemic review and meta-analysis, Eur. Radiol. 29 (2019) 745–758, https://doi.org/10.1007/s00330-018-5608-7.
[33] L. van Santwijk, V. Kouwenberg, F. Meijer, et al., A systematic review and meta-analysis on the differentiation of glioma grade and mutational status by use of perfusion-based magnetic resonance imaging, Insights Imaging 13 (1) (2022) 102, https://doi.org/10.1186/s13244-022-01230-7. Epub 2022/06/08.
[34] S. Ohba, K. Kuwahara, S. Yamada, et al., Correlation between IDH, ATRX, and TERT promoter mutations in glioma, Brain Tumor Pathol. 37 (2) (2020) 33–40, https://doi.org/10.1007/s10014-020-00360-4. Epub 2020/04/01.
[35] P. Yang, J. Cai, W. Yan, et al., Classification based on mutations of TERT promoter and IDH characterizes subtypes in grade II/III gliomas, Neuro Oncol. 18 (8) (2016) 1099–1108, https://doi.org/10.1093/neuonc/now021. Epub 2016/03/10.
[36] K. Leu, G.A. Ott, A. Lai, et al., Perfusion and diffusion MRI signatures in histologic and genetic subtypes of WHO grade II–III diffuse gliomas, Neuro Oncol. 134 (2017) 177–188, https://doi.org/10.1007/s11060-017-2506-9.
[37] F. Arzanforoosh, S.R. van der Voort, F. Incekara, et al., Microvasculature features derived from hybrid EPI MRI in non-enhancing adult-type diffuse glioma subtypes, Cancers 15 (7) (2023), 2135, https://doi.org/10.3390/cancers15072135.
[38] I.J. Pruis, S.R. Koene, S.R. Van Der Voort, et al., Noninvasive differentiation of molecular subtypes of adult nonenhancing glioma using MRI perfusion and diffusion parameters, Neurooncol. Adv. 4 (1) (2022), vdac023, https://doi.org/10.1093/noajnl/vdac023.
[39] K. Wang, Y. Li, H. Cheng, et al., Perfusion CT detects alterations in local cerebral flow of glioma related to IDH, MGMT and TERT status, BMC Neurol. 21 (2021) 1–10, https://doi.org/10.1186/s12883-021-02490-4.
[40] A. Zlochower, D.S. Chow, P. Chang, et al., Deep learning AI applications in the imaging of glioma, Top. Magn. Reson. Imaging. 29 (2) (2020) 115, https://doi.org/10.1097/rmr.0000000000000237. Epub 2020/04/10.
[41] R. Fukuma, T. Yanagisawa, M. Kinoshita, et al., Prediction of IDH and TERT promoter mutations in low-grade glioma from magnetic resonance images using a convolutional neural network, Sci. Rep. 9 (1) (2019) 20311, https://doi.org/10.1038/s41598-019-56767-3. Epub 2020/01/01.
[42] S.R. van der Voort, F. Incekara, M.M.J. Wijnenga, et al., Combined molecular subtyping, grading, and segmentation of glioma using multi-task deep learning, Neuro Oncol. 25 (2) (2023) 279–289, https://doi.org/10.1093/neuonc/noac166. Epub 2022/07/06.
[43] E. Calabrese, J.D. Rudie, A.M. Rauschecker, et al., Combining radiomics and deep convolutional neural network features from preoperative MRI for predicting clinically relevant genetic biomarkers in glioblastoma, Neurooncol. Adv. 4 (1) (2022), vdac060, https://doi.org/10.1093/noajnl/vdac060. Epub 2022/05/26.
[44] X. Ma, K. Cheng, G. Cheng, et al., Apparent diffusion coefficient as imaging biomarker for identifying IDH mutation, 1p19q codeletion, and MGMT promoter methylation status in patients with glioma, J. Magn. Reson. Imaging (2023), https://doi.org/10.1002/jmri.28589. Epub 2023/01/04.
[45] O. Oktay, J. Schlemper, L.L. Folgoc, et al., Attention u-net: learning where to look for the pancreas, arXiv preprint arXiv:180403999, 2018, doi: 10.48550/arXiv.1804.03999.
[46] Z. Liu, Q. Sun, H. Bai, et al., 3D deep attention network for survival prediction from magnetic resonance images in glioblastoma, in: Proceeding of the IEEE International Conference on Image Processing (ICIP), 2019, https://doi.org/10.1109/ICIP.2019.8803077.
[47] J. Cheng, J. Liu, L. Liu, et al., Multi-level glioma segmentation using 3D U-net combined attention mechanism with atrous convolution, in: Proceeding of the IEEE International Conference on Bioinformatics and Biomedicine (BIBM), 2019, https://doi.org/10.1109/BIBM47256.2019.8983092.